

A comparison of prostate cancer bone metastases on ¹⁸F-Sodium Fluoride and Prostate Specific Membrane Antigen (¹⁸F-PSMA) PET/CT: Discordant uptake in the same lesion

Stephanie A. Harmon^{1,2}, Esther Mena², Joanna H. Shih³, Stephen Adler^{1,2}, Yolanda McKinney², Ethan Bergvall², Sherif Mehralivand², Adam G. Sowalsky⁴, Anna Couvillon⁵, Ravi A. Madan⁵, James L. Gulley⁵, Janet Eary⁶, Ronnie C. Mease⁷, Martin G. Pomper⁷, William L. Dahut⁵, Baris Turkbey², Liza Lindenberg² and Peter L. Choyke²

¹Clinical Research Directorate, Frederick National Laboratory for Cancer Research sponsored by the National Cancer Institute, Frederick, MD, USA

²Molecular Imaging Program, National Cancer Institute, NIH, Bethesda, MD, USA

³Biometric Research Branch, National Cancer Institute, NIH, Bethesda, MD, USA

⁴Laboratory of Genitourinary Cancer Pathogenesis, Center for Cancer Research, National Cancer Institute, NIH, Bethesda, MD, USA

⁵Genitourinary Malignancies Branch, National Cancer Institute, NIH, Bethesda, MD, USA

⁶Cancer Imaging Program, National Cancer Institute, NIH, Rockville, MD, USA

⁷Russell H. Morgan Department of Radiology and Radiological Science, Johns Hopkins University School of Medicine, Baltimore, MD, USA

Correspondence to: Stephanie A. Harmon, **email:** stephanie.harmon@nih.gov

Keywords: prostate cancer; bone metastases; sodium fluoride; prostate specific membrane antigen; spatial analysis

Received: October 01, 2018

Accepted: December 04, 2018

Published: December 28, 2018

Copyright: Harmon et al. This is an open-access article distributed under the terms of the Creative Commons Attribution License 3.0 (CC BY 3.0), which permits unrestricted use, distribution, and reproduction in any medium, provided the original author and source are credited.

ABSTRACT

Purpose: Prostate-Specific Membrane Antigen (PSMA) PET/CT has been introduced as a sensitive method for characterizing metastatic prostate cancer. The purpose of this study is to compare the spatial concordance of ¹⁸F-NaF PET/CT and ¹⁸F-PSMA-targeted PET/CT within prostate cancer bone metastases.

Methods: Prostate cancer patients with known bone metastases underwent PSMA-targeted PET/CT (¹⁸F-DCFBC or ¹⁸F-DCFPyL) and ¹⁸F-NaF PET/CT. In pelvic and spinal lesions detected by both radiotracers, regions-of-interest (ROIs) derived by various thresholds of uptake intensity were compared for spatial colocalization. Overlap volume was correlated with uptake characteristics and disease status.

Results: The study included 149 lesions in 19 patients. Qualitatively, lesions exhibited a heterogeneous range of spatial concordance between PSMA and NaF uptake from completely matched to completely discordant. Quantitatively, overlap volume decreased as a function of tracer intensity and disease status, where lesions from patients with castration-sensitive disease showed higher spatial concordance while lesions from patients with castration-resistant disease demonstrated more frequent spatial discordance.

Conclusion: As metastatic prostate cancer progresses from castration-sensitive to castration-resistant, greater discordance is observed between NaF PET and PSMA PET uptake. This may indicate a possible phenotypic shift to tumor growth that is more independent of bone remodeling via osteoblastic formation.

INTRODUCTION

Most men who develop metastatic prostate cancer in the bone inevitably succumb to the disease [1]. It is thought that once seeding of prostate cancer cells within the bone has occurred and formation of metastasis begins, continued growth and proliferation of cancer cells is dependent on a complex interaction between the cancer cells and the bone microenvironment, leading to a 'vicious cycle' of osteoblast recruitment and osteoclastic response within the local area of metastatic invasion [2]. This eventually leads to the osteosclerotic lesion associated with prostate cancer metastases. Radionuclide bone scans have long been regarded as a reliable modality for imaging bone metastases due to their sensitivity in detecting regions of high bone turnover. Several types of bone scans are currently available including ^{99m}Tc methylene diphosphonate (MDP) planar bone scans, which are the traditional method, and relatively newer techniques such as ^{99m}Tc -MDP SPECT/CT and ^{18}F -NaF PET/CT which show superior detection sensitivity [3, 4]. These agents are all taken up in areas of active bone remodeling, specifically new bone formation indicating increased osteoblast activity by osteocytes that are actively laying down bone.

Recently, prostate cancer imaging agents targeting Prostate Specific Membrane Antigen (PSMA), which is highly expressed in prostate cancer cells, have become available. PSMA contains a carboxypeptidase that is thought to cleave glutamate from vitamin B9, possibly activating the phosphoinositide 3-kinase pathway and promoting prostate cancer growth independent of the androgen receptor (AR) pathway [5]. Several PSMA-targeted radiotracers are in clinical trials evaluation, all of which bind to the enzymatic region of PSMA with high affinity and target viable tumor providing a unique biomarker for metastatic disease [6–8].

Previous reports have indicated that there are discrepancies in detection of bone metastases between bone imaging agents and PSMA agents in metastatic prostate cancers [9–14]. These discrepancies are reported *at the lesion level*, i.e. a lesion is seen either on one but not the other. This may depend on disease status (PSMA expressing or not) and the effects of therapy such as suppression of the AR pathway with androgen deprivation therapy (ADT) [12]. However, so far little attention has been paid to spatial colocalization of ^{18}F -NaF PET/CT and PSMA PET/CT uptake *within* the same bone lesion. While the microenvironment within prostate cancer bone metastases contains both osteocytes and cancer cells, the presence and degree to which they co-localize has yet to be functionally evaluated across individual lesions. Given the different targeting mechanisms it is feasible uptake distributions may be different within the same lesion, and findings of spatial discordance have potential therapeutic implications for patients with bony prostate

metastases. In this study, uptake by both PET/CT agents within individual lesions were carefully mapped by CT co-registration with the purpose to characterize the degree of spatial concordance between ^{18}F -NaF PET and ^{18}F -PSMA PET uptake.

RESULTS

Fifty-two patients with metastatic prostate cancer were enrolled across both imaging studies. Nineteen patients met study inclusion criteria with bone metastases in the pelvis or spine co-detected by NaF PET/CT and PSMA PET/CT. Patients were excluded based on soft tissue only disease (N=9), patients with NaF-only bone lesions (N=14), patients with negative scans (N=7), or patients with co-detected lesions not meeting inclusion criteria (N=6). A summary of patient demographics and lesion characteristics are listed in Table 1, with patient-specific characteristics listed in Supplementary Table 1.

224 prostate cancer bone metastases were detected by both NaF and PSMA imaging. 149 of these lesions met inclusion criteria for analysis. Qualitatively, metastases visually exhibited various degrees of matching between the two scan types, as summarized in Figures 1-3. While some lesions demonstrated nearly complete concordance (Figure 1A, 1B) of uptake, others showed regionally-similar distribution manifested as moderate (Figure 2A) or high (Figure 2B) concordance. This further devolved into patterns where partial (Figure 3B) to substantial (Figure 3C) spatial uptake discordance was observed.

Robust CT registration between NaF PET/CT and PSMA PET/CT imaging studies allowed robust registration as was demonstrated by an ICC of 0.926. In the mixed effects model of CT characteristics, Hounsfield Unit (HU) values were shown to vary regionally within voxels categorized by which types of ROIs they were contained within (Table 2). Voxels contained only within PSMA ROIs demonstrated the lowest HU, indicating less sclerosis, while voxels contained only within CT ROIs demonstrated the highest HU (Supplementary Figure 1). Only one lesion in this patient population was characterized by true osteolytic appearance, demonstrating poor spatial colocalization (Supplemental Figure 2).

Similar to the qualitative findings, concordance of NaF and PSMA ROI volumes varied substantially across all lesions, with median overlap volume 0.77 (range 0-1). PSMA ROIs showed higher concordance with NaF ROIs compared to CT ROIs ($p=0.047$), while NaF volumes showed similar spatial overlap with CT (median 0.75, range 0-1) as observed with NaF and PSMA volumes (Supplementary Figure 3). Lesions within the same patient showed varying degrees of spatial discordance and patient-level heterogeneity was observed across metastatic burden (Supplementary Figure 4).

ROI volumes of each bone lesion were further segmented at multiple uptake intensity levels, as

Table 1: Patient Demographics

Metric	Summary
N patients	19
PSA (ng/mL)	9.17 (0.27->5000)
Status	
CRPC	13
CSPC	6
Treatment History	
Untreated	1
Radical Prostatectomy	8
Radiation Therapy	12
Androgen-targeted Therapy	17
Chemotherapy	9
²²³ Ra	2
N lesions detected by both	
Total*	167+
per patient	(1-100+)
N lesions included in analysis	
total	149
per patient	5 (1-20)
Bone regions	
Ilium	29
Thoracic Spine	41
Lumbar Spine	35
Sacrum	17
Pubis/Ischium	19
Acetabulum	3
Cervical Spine	2
Humeral Head	2
Femoral Head	1

*In three patients, true burden estimation was not quantifiable due to N>100 detected lesions by either tracer.

described in Figure 4. In this analysis, overlap between NaF and PSMA volumes decreased incrementally at image intensity thresholds of 60%-SUV_{max} (p=0.002), 70%-SUV_{max} (p=0.0005), and 80%-SUV_{max} (p=0.0008). This finding varied according to whether patients were considered to have castration-sensitive (N=6) vs. castration-resistant (N=13) disease, as shown in Figure 5. Metastatic bone lesions in patients with castrate-sensitive disease maintained moderate spatial concordance across all intensity threshold levels (median 62.5% in

80%-SUV_{max} ROIs) while the degree of overlap in lesions within patients with castration-resistant disease decreased significantly at each intensity level (median 21.5% in 80%-SUV_{max} ROIs). Overlap volume in the castration-sensitive group was modestly higher than the castrate-resistant group at 60%-SUV_{max} (p=0.15), becoming significant at 70%-SUV_{max} (p=0.02) and 80%-SUV_{max} (p=0.004). Distance metrics between areas of highest uptake in NaF and PSMA additionally show higher separation (more discordance) in CRPC patients (Table 3).

Correlation between overlap volume, PET uptake from both radiotracers, and CT characteristics are summarized in Supplementary Table 2. Overlap volume showed weak-to-no correlation to NaF ROI volume

($\rho=0.20$) and PSMA ROI volume ($\rho=0.29$), remaining so at all levels of intensity segmentation. Weak-to-moderate inverse correlation was observed for overlap volumes at all image segmentation levels vs. SUV_{max} of NaF, ranging

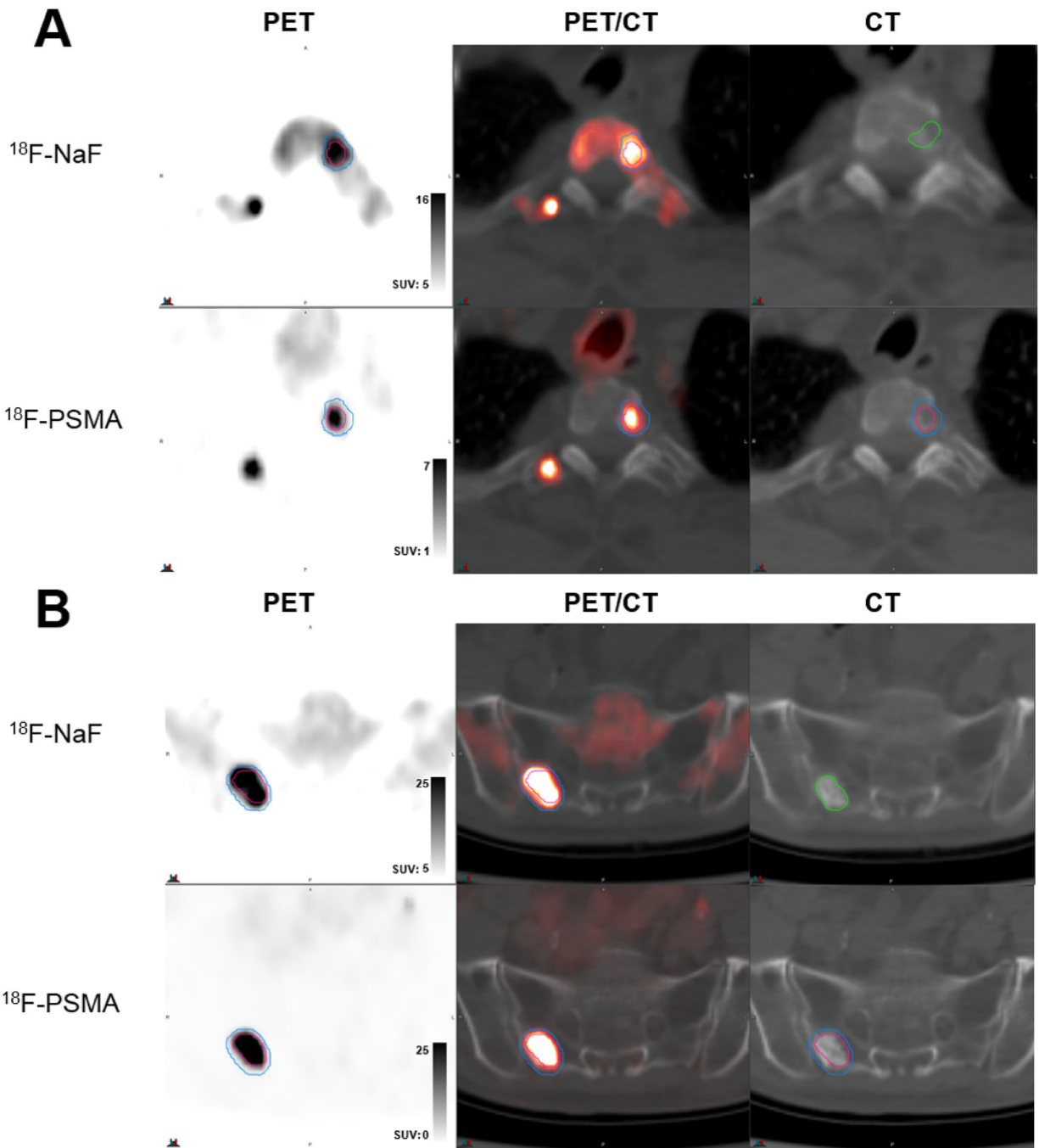


Figure 1: Examples of high volume and spatial uptake concordance. (A) Lesion in T2 spine of patient newly diagnosed with de novo metastatic disease (serum PSA 16 ng/ml) demonstrating 100% volumetric overlap between ^{18}F -NaF uptake (top row, blue contour) and ^{18}F -PSMA (DCFpYL) (bottom row, red contour) uptake, with CT contour shown in green. (B) Lesion in sacrum of castrate-sensitive patient (serum PSA 3.05 ng/ml) demonstrating 88.7% volumetric overlap between ^{18}F -NaF uptake (top row, blue contour) and ^{18}F -PSMA (DCFpYL) (bottom row, red contour) uptake, with CT contour shown in green. In both (A) and (B), top row demonstrates PET uptake, PET/CT overlay, and low-dose CT from ^{18}F -NaF scan and bottom row demonstrates PET uptake, PET/CT overlay, and low-dose CT from ^{18}F -PSMA (DCFpYL) scan with registered contour overlay.

from -0.09 to 0.23, and PSMA, ranging from -0.03 to -0.29 (Supplementary Table 2). A modest, association between HU_{mean} and overlap volume was observed at all PSMA segmentation levels (ranging from $\rho=0.31$ to 0.36).

No correlation was demonstrated for SUV_{max} and HU_{mean} between PET imaging agents and any segmentation level (Supplementary Table 3).

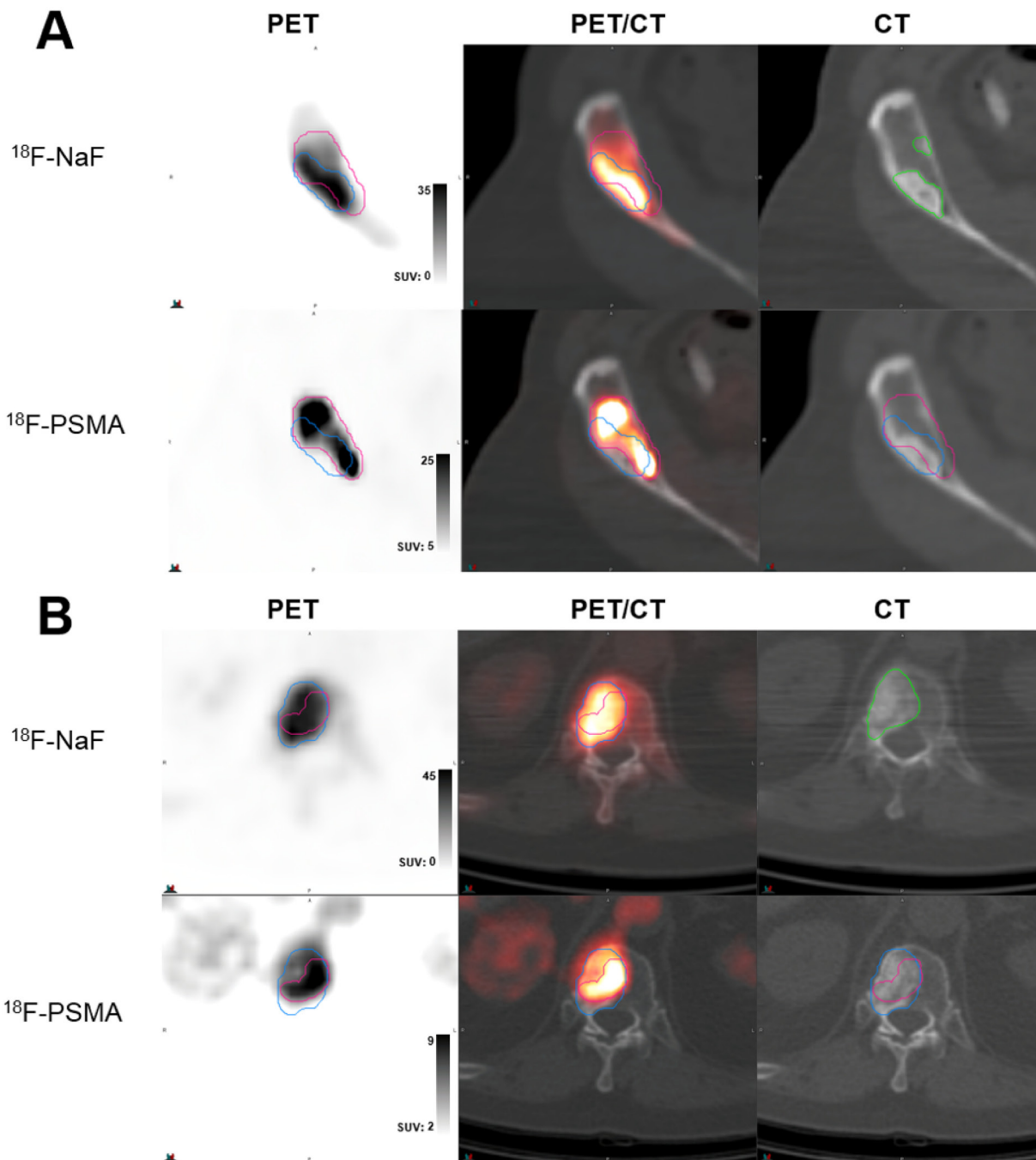


Figure 2: Examples of moderate-to-high volume concordance, with differential localization of highest uptake. (A) Lesion in anterior iliac crest of castrate-resistant patient (serum PSA 93.3 ng/ml) demonstrating moderate 74.9% volumetric overlap between ^{18}F -NaF uptake (top row, blue contour) and ^{18}F -PSMA (DCFpyL) (bottom row, red contour) uptake, but mismatching patterns of high uptake within contours and areas of sclerosis on CT (green contour). **(B)** Lesion in T12 spine of castrate-resistant patient (serum PSA 388.1 ng/ml) demonstrating high 95.5% volumetric overlap between ^{18}F -NaF uptake (top row, blue contour) and ^{18}F -PSMA (DCFBC) (bottom row, red contour) uptake within visible CT lesion (green contour), but differential areas of highest uptake. In both (A) and (B), top row demonstrates PET uptake, PET/CT overlay, and low-dose CT from ^{18}F -NaF scan and bottom row demonstrates PET uptake, PET/CT overlay, and low-dose CT from PSMA scans with registered contour overlay.

DISCUSSION

This study demonstrates that many prostate bone metastases are moderately to highly discordant in regard to regions of uptake of ^{18}F -NaF PET and ^{18}F -PSMA. It is well

established that prostate cancer bone metastases induce an osteoblastic bone reaction, visible on bone scans and CT imaging [15]. However, this does not imply perfect concordance between areas of high bone turnover and areas of highest cancer activity. Indeed, it is a common

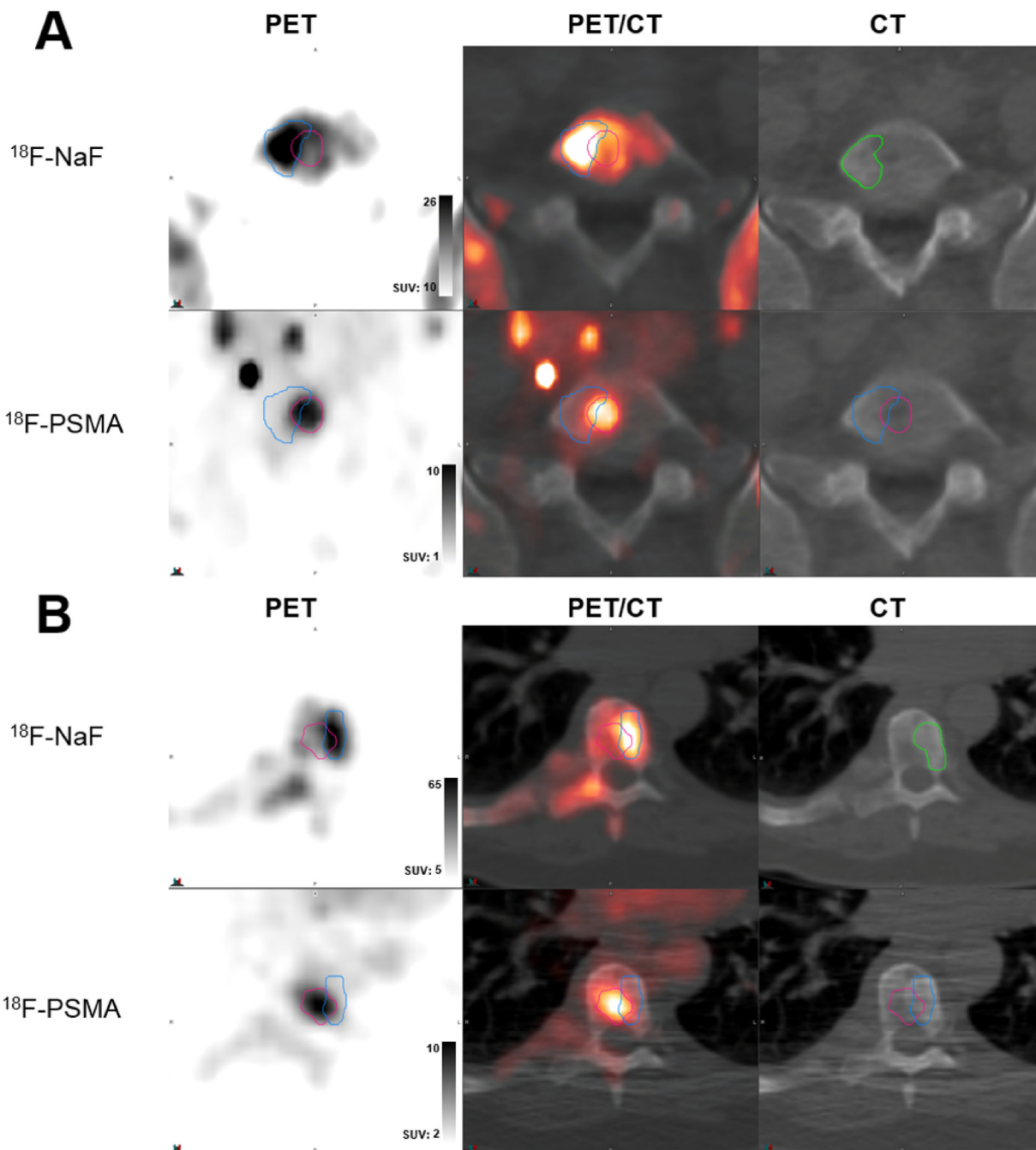


Figure 3: Examples of low volume and spatial uptake concordance. (A) Lesion in L5 spine of castrate-resistant patient (serum PSA 11.79 ng/ml) demonstrating poor 62.2% volumetric overlap between ^{18}F -NaF uptake (top row, blue contour) and ^{18}F -PSMA (DCFPyL) (bottom row, red contour) uptake, with marked mismatching patterns of high uptake within contours. (B) Lesion in T12 spine of castrate-resistant patient (serum PSA 4379 ng/ml) demonstrating high 30.9% volumetric overlap between ^{18}F -NaF uptake (top row, blue contour) and ^{18}F -PSMA (DCFBC) (bottom row, red contour) uptake, with substantial mismatch in uptake patterns. In both (A) and (B), top row demonstrates PET uptake, PET/CT overlay, and low-dose CT from ^{18}F -NaF scan and bottom row demonstrates PET uptake, PET/CT overlay, and low-dose CT from PSMA scans with registered contour overlay. CT contours shown in green.

Table 2: Summary of fixed effects estimate from linear mixed effects model of CT (HU) characteristics measured by CT scans acquired during PSMA and NaF PET sessions, using nested random effects model for lesion-based voxel dependencies

Region of overlap	Estimate	SE	p-value
CT exclusive	38.6	1.4	<0.001
NaF-CT only	33.2	1.5	<0.001
PSMA, NaF, and CT	518		reference
PSMA-CT only	-31.7	2.0	<0.001
NaF exclusive	-179	1.4	<0.001
PSMA-NaF only	-206	1.5	<0.001
PSMA exclusive	-272	1.4	<0.001

Region of overlap was assigned as one of 7 possible categorical memberships for each voxel, using voxels contained within all ROIs (PSMA, NaF, CT) as reference for comparison.

experience that biopsies of sclerotic or bone scan-positive lesions for pathological confirmation of metastatic disease are often negative [16]. While the presence of enhanced bone activity and formation is known to exist in metastatic sites, the spatial concordance with cancer cells has not been functionally evaluated. In this analysis, we report a highly variable spatial concordance of NaF and PSMA PET uptake within the same bone metastases, in which the

degree of discordance increases as the disease progresses to castration-resistance.

The disturbance of normal bone homeostasis and active remodeling in sites of skeletal metastatic disease occurs early in the prostate cancer metastatic process and persists throughout the disease, resulting in predominately osteoblastic bone lesions [2, 17]. This knowledge has led to use of the standard MDP bone scan and ¹⁸F-NaF PET/

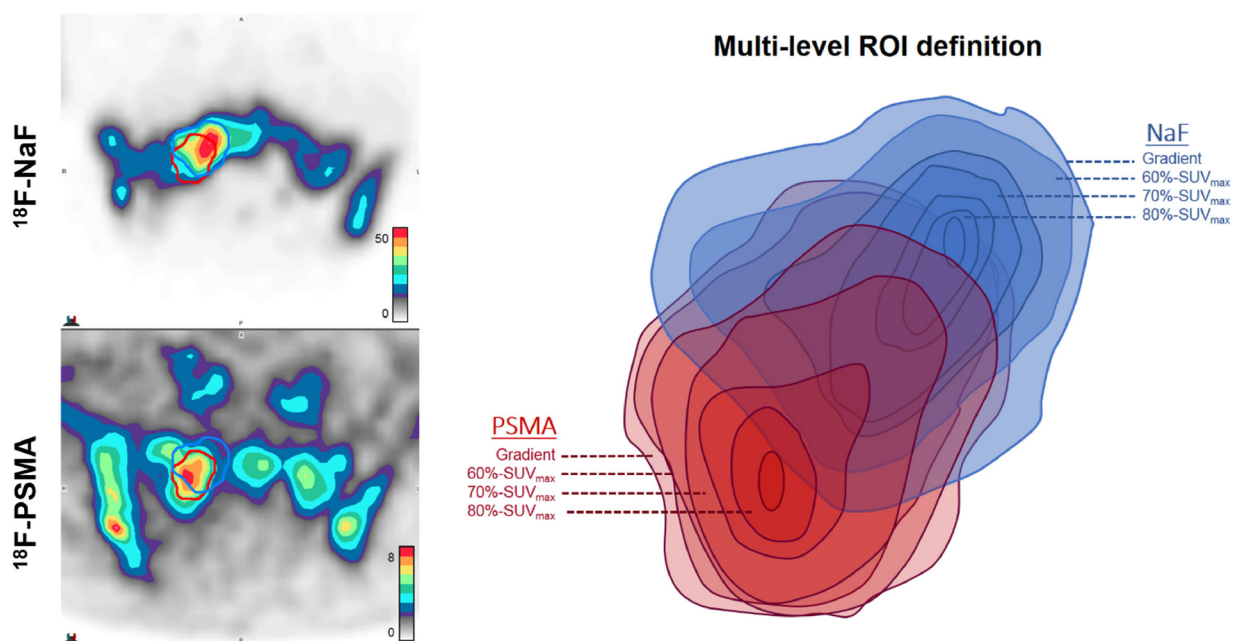


Figure 4: Illustrative example of multi-level segmentation by tracer activity. Gradient-based segmentation (outermost level) demonstrates moderate spatial concordance of ROI volumes in right sacral bone lesion of castration-resistant patient (serum PSA 4379 ng/ml) imaged with ¹⁸F-PSMA (DCFBC) and ¹⁸F-NaF. For each radiotracer, additional ROIs are then derived from voxels within gradient-based volumes that fall within 60% of SUV_{max} , 70% of SUV_{max} and 80% of SUV_{max} . Thus, each ROI is incrementally smaller in volume and higher in uptake relative to SUV_{max} of each tracer within each bone lesion. The example provided demonstrates spatially discordant regions of highest uptake, with decreasing areas of ROI overlap at increasing levels of relative tracer intensity.

CT for patient assessment. These imaging agents target areas of increased bone turnover and new bone formation [18]. Spatially, this interaction of prostate cancer cells with the bone microenvironment coincides, such that the region of active bone remodeling usually reflects the region of active cancer [17]. This theory is supported by several findings that tumor burden in a metastatic lesion is regulated by tumor cell interactions with cells within the bone microenvironment, which includes osteoblasts, osteoclasts, and bone stromal cells [19–22]. We find high spatial concordance of osteoblastic activity and cancer-specific PSMA activity occurs more frequently in early (castrate-sensitive) disease.

Lesions in patients with advanced castration-resistant disease [23], show more discordance between regions of osteoblastic activity and PSMA positive tissue. These findings could support the theory that the heterogeneous nature of metastatic prostate cancer, while driven by osteoblastic response initially, eventually evolves to become independent of an osteoblastic response [20], leading to dynamic pathobiologic diversity in end-stage disease [24]. High PSMA PET uptake in areas

suspicious for metastasis is considered highly reliable for prostate cancer and discordance with NaF can be interpreted to suggest there is an invasive component not driven by osteoblastic reaction. This parallels bone findings in metastatic breast cancer, where predominately osteolytic mechanisms are suspected to underlay observed discordance between NaF PET/CT and FDG PET/CT [25, 26].

These findings have potential clinical relevance with regard to recently developed therapies for metastatic prostate cancer. ^{223}Ra has been approved for treatment of metastatic bone disease [27]. Preliminary studies show spatial correlation between ^{18}F -NaF PET/CT uptake and ^{223}Ra deposition [28]. Since ^{223}Ra is an alpha emitter its region of therapeutic efficacy is narrowly defined (within only a few cell diameters), Use in patients with a high degree of spatial discordance between ^{18}F -NaF and ^{18}F -PSMA could potentially result in undertreatment of disease within these lesions.

Different pairs of PSMA PET and bone scan agents have shown differing detection performance of metastatic bone disease in the past [11–13]. Similar detection

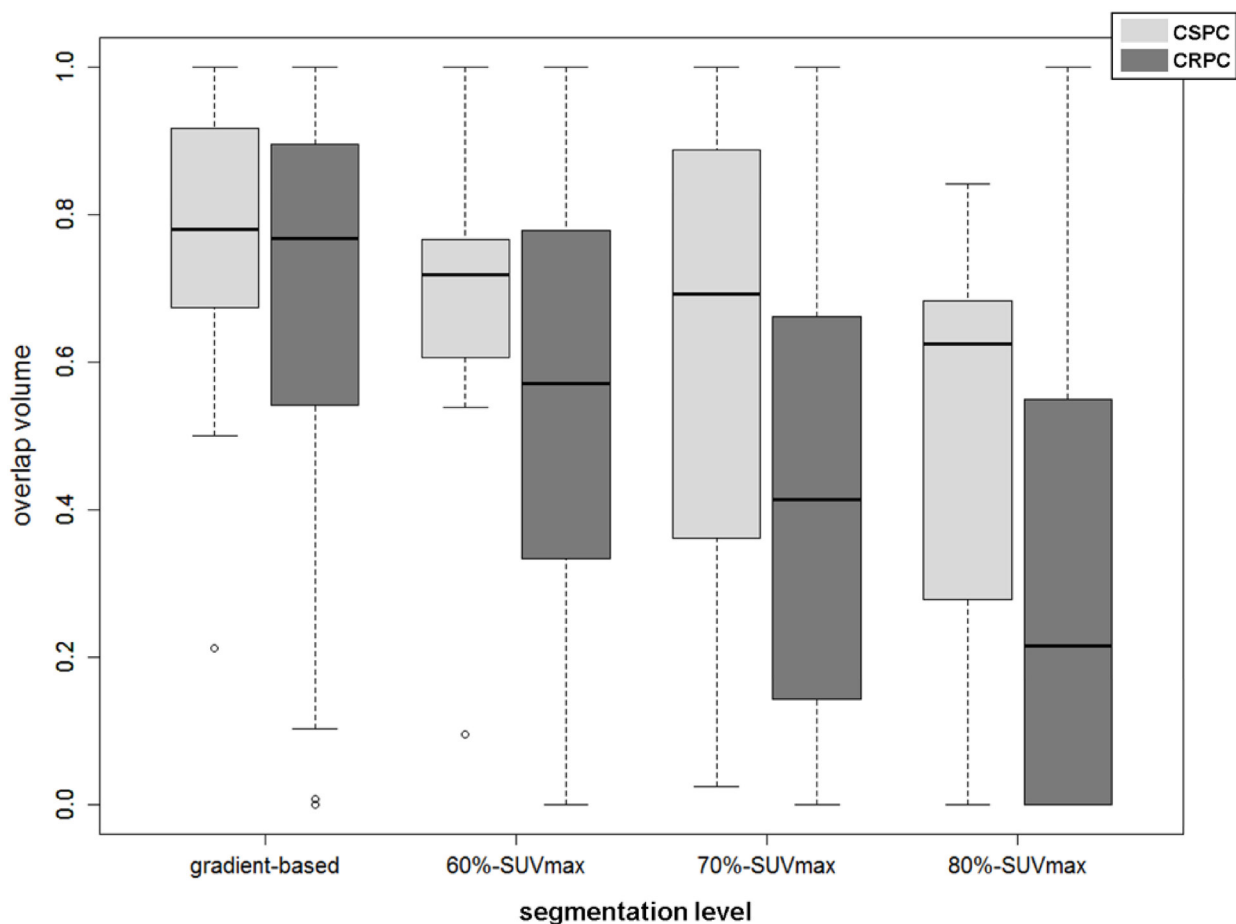


Figure 5: Overlap Volume (OV) vs. segmentation level for CRPC and CSPC patients at various segmentation levels, demonstrating increased spatial discordance at higher levels of tracer activity ranging from gradient-based demonstrating no significant difference ($p>0.2$), 60%-SUV_{max} ROIs ($p=0.15$), 70%-SUV_{max} ROIs ($p=0.02$), and 80%-SUV_{max} ROIs ($p=0.0035$).

Table 3: Distance measures for CRPC (N = 13) and CSPC (N = 6) patients

Distance Measure	CSPC median (range)	CRPC median (range)	p-value
Distance (mm) between SUV _{max}	3.80 (1.94-11.7)	8.91 (0-60.3)	0.001
distance (mm) between 80%-SUV _{max} ROI centroids	2.45 (1.1-5.2)	6.56 (1.0-29.7)	0.002
average pairwise distance (mm) between 80%-SUV _{max} ROIs	4.2 (2.3-10.3)	10.4 (2.8-37.6)	<0.001

Significance was evaluated by permutation test accounting for intra-patient correlations.

differences with other PET agents used in metastatic prostate cancer have been reported [29–31]. These findings are likely the result of complex interactions between treatment timing/effect and disease state, underscoring the need for reliable imaging biomarkers throughout the course of disease. In the absence of histological validation for all lesions, inclusion of lesions detected by both tracers allows for phenotypic comparisons within lesions most likely to contain metastatic prostate cancer. Several studies indicate that CT appearance and density correlates to differences in uptake between various radiotracers [31, 32], demonstrating NaF has a higher tumor-to-background ratio in osteosclerotic lesions [13]. Our voxel-based analysis are in general agreement, demonstrating regions defined only by PSMA uptake associate with regions of lower HU.

This study has several limitations. Accurate image segmentation for bone lesions remains an ongoing issue in PET/CT. To account for this fact, multiple image intensity based segmentations were performed in this study to investigate colocalization of tracer uptake without dependency on tumor volume or extent. No partial volume corrections were made, though both cohorts were reconstructed using time-of-flight algorithms, which in combination with point-spread function modeling, may limit the influence of partial volume effects [33]. It is unclear the presence or density of tumor cells and osteoid components within these phenotypic regions. The resolution of PET limits the detection capabilities to the extent that could be achieved in histopathological analysis; however, tissue-based sampling in all metastatic sites is infeasible. Furthermore, the influence of treatment status at the time of imaging on the colocalization of tracers could not be evaluated in this small cohort. A disproportionate number of castration-sensitive patients were in the DCFPyL cohort (6/7); however, similar rates of decreasing overlap volume were observed between imaging cohorts (Supplementary Figure 5). Longitudinal assessment at multiple timepoints by these tracers would be helpful to understand the dynamics of disease activity and tracer uptake over time.

In conclusion, ¹⁸F-NaF and ¹⁸F-PSMA PET scans for metastatic prostate cancer can show considerable discordance in regions of increased uptake within a bone metastasis. The relationship between PSMA activity in prostate metastases and bone turnover appears to become weaker in more advanced stages of disease, with metastases occupying portions of bone with no apparent bone turnover or osteoblastic proliferation. In addition to possibly providing insights into the evolution of prostate cancer metastatic spread, these findings have potential implications for radionuclide therapies such as ²²³Ra that depend on localization in areas of increased bone turnover.

MATERIALS AND METHODS

Patient population

This study population includes patients with known metastatic prostate cancer undergoing PSMA-targeted PET/CT, using either ¹⁸F-DCFBC PET/CT imaging (NCT02190279) or ¹⁸F-DCFPyL PET/CT imaging (NCT03173924), and NaF PET/CT for metastatic disease assessment at a single institution. These studies were approved by the Institutional Review Board and were Health Insurance Portability and Accountability Act compliant. All patients enrolled after written informed consent was obtained. Eligibility required histopathologically confirmed prostate cancer and identifiable metastatic disease on conventional imaging (CT, magnetic resonance imaging or bone scan). All patients received ¹⁸F-DCFBC PET/CT or ¹⁸F-DCFPyL PET/CT and ¹⁸F-NaF PET/CT scans. Clinical demographics, including castration sensitivity/resistance status and prior treatment history were established based on clinical review of patient medical records.

Image acquisition

Patients imaged between 2014-2016 underwent ¹⁸F-DCFBC PET/CT and ¹⁸F-NaF PET/CT scanning (median interval 1 day, range 1-25), as described

previously [12]. Patients received ^{18}F -DCFBC administered as an IV bolus (median injected dose 8mCi [7.5-8 mCi]) followed by a static whole-body PET/CT performed at 120 minutes post-injection. ^{18}F -NaF was commercially obtained (Cardinal Health, Greenbelt, MD). A single, static whole body ^{18}F -NaF PET/CT scan was performed 60 minutes after IV bolus (median injected dose 3.5 mCi [3.4-3.6 mCi]) of radiotracer. All imaging was performed on a Philips Gemini TF system (Philips Health Care, Cleveland, OH, USA). Low-dose CT transmission scans were obtained (120 kVp, 60mAs, 0.75 second rotation time, 1.438 pitch, axial slice thickness of 5mm) for attenuation correction and localization. Emission PET images were obtained at 2 minutes/bed position with 22 slices in bed overlap. The PET images were reconstructed using the Gemini TF [34] default reconstruction algorithm (BLOB-OS-TF, a 3D ordered subset iterative TOF reconstruction technique using 3 iterations, 33 subsets, voxel size $4 \times 4 \times 4 \text{ mm}^3$).

Patients imaged between 2017-2018 underwent ^{18}F -DCFPyL PET/CT and ^{18}F -NaF PET/CT scanning (median interval 1 day, range 1-19). Production of ^{18}F -DCFPyL, a second generation version of ^{18}F -DCFBC, has been described previously [35]. Patients received ^{18}F -DCFPyL administered as an IV bolus (median injected dose 8.25mCi [8.1-8.4 mCi]) followed by a static whole-body PET/CT performed at 120 minutes post-injection. The ^{18}F -NaF imaging procedure was identical for both patient PSMA scan groups (median injected dose 3.46 mCi [3.1-5mCi]). Imaging was performed on a GE Discovery MI DR system (General Electric Medical Systems, Waukesha, WI, USA). Low-dose CT transmission scans were obtained (120 kVp, 2mAs, 0.5 second rotation time, 0.9844 pitch, axial slice thickness of 3.75mm) for attenuation correction and localization. Emission PET images were obtained at 3 minutes/bed position with 22 slices in bed overlap. PET images were reconstructed using Q. Clear method, a Bayesian penalized-likelihood TOF reconstruction algorithm with voxel size $2.73 \times 2.73 \times 3.27 \text{ mm}^3$.

^{18}F -DCFBC, a first generation agent, suffered from relatively high retention in the blood resulting in slower clearance compared to ^{18}F -DCFPyL [6]. However, as ^{18}F -DCFPyL and ^{18}F -DCFBC agents are chemically related and bind with high affinity to the same PSMA epitope on prostate cancer cells, they are referred to collectively as ^{18}F -PSMA scans in this analysis.

Lesion-based inclusion criteria and image analysis

Standardized Uptake Values (SUVs) were calculated as the ratio of measured activity to injected dose per body weight (kilogram). Image review and analysis was performed using commercial software (MIM v.6.6.10, Cleveland, OH, USA). Lesions

determined to be highly suspicious for metastatic disease by consensus of 3 nuclear medicine physicians were considered for analysis. Of highly suspicious bone lesions detected both by NaF PET/CT and PSMA-targeting PET/CT, only those within the pelvis and spine were included in spatial analysis to reduce artifacts introduced from breathing motion (ribs) or patient-positioning motion (extremities, skull). Regions-of-interest (ROI) for each tracer were obtained by semi-automated gradient-based method (PETEdge, MIM). ROIs were further segmented into areas of highest tracer uptake by 60%, 70% and 80% thresholds of lesion-specific SUV_{max} , as described in Figure 4. Regions corresponding to PET-detected lesions were segmented by CT appearance, i.e. encompassing radiographic visibility, by nuclear medicine specialists.

A two-step image registration procedure was completed using low dose CTs. First global skeletal alignment was achieved using rigid alignment. Next, lesion-based alignment was further achieved using local box-based optimization fit to bony regions containing each lesion (Box-based Assisted Alignment, MIM). After registration, spatial concordance of NaF and PSMA ROIs was evaluated by assessing the degree of overlap volume in the area of increased radiotracer uptake, defined as the ratio of overlapping volume to minimum lesion volume. This calculation was repeated for NaF and PSMA overlap with CT. Each voxel was assigned to one of seven possible concordance categories: PSMA exclusive, NaF exclusive, CT exclusive, PSMA and NaF only, PSMA and CT only, NaF and CT only, or all matching (included in all PSMA, NaF, and CT). Distance between regions of highest tracer uptake was measured by, absolute distance from PSMA SUV_{max} and NaF SUV_{max} . To avoid potential bias from partial-volume errors, the distance between center-of-mass and average pairwise distance from 80%- SUV_{max} PSMA ROIs and 80%- SUV_{max} NaF ROIs were also calculated.

Statistical analysis

Voxel-based accuracy of lesion-specific registration was evaluated using the Intraclass Correlation Coefficient (ICC), estimated from a mixed effect model of Hounsfield Units (HU) measurements with nested random effects for patient, lesions, skeletal region and PSMA tracers (DCFBC or DCFPyL) and fixed effect voxel-based concordance category. The significance of fixed effects was determined by the likelihood ratio test. Differences in lesion-based overlap volume as a function of ROI segmentation method was evaluated using paired Wilcoxon signed-rank test using Rosner–Glynn–Lee method to account for intra-patient correlation [36]. Association of overlap volume and distance metrics with disease status (castration-sensitive vs. castration-resistant) was evaluated by

permutation test with 2000 permutations at the patient level. Correlation between SUV metrics, PET tumor uptake volume, and CT characteristics were completed using the Spearman correlation coefficient. Standard errors and 95% confidence intervals (CI) were estimated from 2000 bootstrap samples by random sampling on the patient-level. All p-values correspond to two-sided tests, with a p-value <0.05 considered to represent a significant difference between results.

Author contributions

Author	Design	Radio-pharmaceutical Development	Patient Monitoring	Data acquisition (imaging)	Data Analysis and Interpretation	Statistics	Manuscript preparation/editing	Manuscript Approval
Stephanie A Harmon					X	X	X	X
Esther Mena	X			X	X		X	X
Joanna H. Shih	X				X	X	X	X
Stephen Adler				X	X		X	X
Yolanda McKinney			X	X			X	X
Ethan Bergvall				X	X		X	X
Sherif Mehrlivand					X		X	X
Adam G Sowalsky					X		X	X
Anna Couvillon			X				X	X
Ravi A Madan			X				X	X
James L Gulley			X				X	X
Janet Eary							X	X
Ronnie C Mease		X					X	X
Martin G Pomper	X	X			X		X	X
William L Dahut			X				X	X
Baris Turkbey	X			X	X		X	X
M Liza Lindenberg	X			X	X		X	X
Peter L Choyke	X			X	X		X	X

ACKNOWLEDGMENTS

The authors would like to thank Anita Ton, Juanita Weaver, Phillip Eclarinal, and Alicia Forest for their contribution to image acquisition.

CONFLICTS OF INTEREST

MGP and RCM are co-inventors on a U.S. patent covering ¹⁸F-DCFPyL and as such is entitled to a portion of any licensing fees and royalties generated by this technology. This arrangement has been reviewed and

Abbreviations

PSMA: Prostate Specific Membrane Antigen; NaF: Sodium Flouride; CT: Computed Tomography; SUV: Standardized Uptake Value; HU: Hounsfield Unit; ICC: Intraclass Correlation Coefficient; ROI: Region of interest; MDP: methylene diphosphonate; AR: Androgen Receptor; CRPC: Castrate-Resistant Prostate Cancer; CSPC: Castrate-Sensitive Prostate Cancer

approved by the Johns Hopkins University in accordance with its conflict-of-interest policies.

FUNDING

This project has been funded in whole or in part with federal funds from the National Cancer Institute, National Institutes of Health, under Contract No. HHSN261200800001E. The content of this publication does not necessarily reflect the views or policies of the Department of Health and Human Services, nor does mention of trade names, commercial products, or

organizations imply endorsement by the U.S. Government. This project was supported in part by the Intramural Research Program of the NIH and NIH grants CA134675, CA183031, and EB024495.

REFERENCES

1. Wu JN, Fish KM, Evans CP, Devere White RW, Dall'Era MA. No improvement noted in overall or cause-specific survival for men presenting with metastatic prostate cancer over a 20-year period. *Cancer*. 2014; 120:818-23. <https://doi.org/10.1002/cncr.28485>.
2. Ibrahim T, Flamini E, Mercatali L, Sacanna E, Serra P, Amadori D. Pathogenesis of osteoblastic bone metastases from prostate cancer. *Cancer*. 2010; 116:1406-18. <https://doi.org/10.1002/cncr.24896>.
3. Iagaru A, Mittra E, Dick DW, Gambhir SS. Prospective Evaluation of Tc-99m MDP Scintigraphy, F-18 NaF PET/CT, and F-18 FDG PET/CT for Detection of Skeletal Metastases. *Molecular Imaging and Biology*. 2012; 14:252-9. <https://doi.org/10.1007/s11307-011-0486-2>.
4. Even-Sapir E, Metsker U, Mishani E, Lievshitz G, Lerman H, Leibovitch I. The detection of bone metastases in patients with high-risk prostate cancer: 99mTc-MDP Planar bone scintigraphy, single- and multi-field-of-view SPECT, 18F-fluoride PET, and 18F-fluoride PET/CT. *J Nucl Med*. 2006; 47:287-97.
5. Kaittani C, Andreou C, Hieronymus H, Mao N, Foss CA, Eiber M, Weirich G, Panchal P, Gopalan A, Zurita J, Achilefu S, Chiosis G, Ponomarev V, et al. Prostate-specific membrane antigen cleavage of vitamin B9 stimulates oncogenic signaling through metabotropic glutamate receptors. *J Exp Med*. 2018; 215:159-75. <https://doi.org/10.1084/jem.20171052>.
6. Szabo Z, Mena E, Rowe SP, Plyku D, Nidal R, Eisenberger MA, Antonarakis ES, Fan H, Dannals RF, Chen Y, Mease RC, Vranesic M, Bhatnagar A, et al. Initial Evaluation of [(18F)]DCFPyL for Prostate-Specific Membrane Antigen (PSMA)-Targeted PET Imaging of Prostate Cancer. *Mol Imaging Biol*. 2015; 17:565-74. <https://doi.org/10.1007/s11307-015-0850-8>.
7. Afshar-Oromieh A, Holland-Letz T, Giesel FL, Kratochwil C, Mier W, Haufe S, Debus N, Eder M, Eisenhut M, Schafer M, Neels O, Hohenfellner M, Kopka K, et al. Diagnostic performance of 68Ga-PSMA-11 (HBED-CC) PET/CT in patients with recurrent prostate cancer: evaluation in 1007 patients. *Eur J Nucl Med Mol Imaging*. 2017; 44:1258-68. <https://doi.org/10.1007/s00259-017-3711-7>
8. Eiber M, Fendler WP, Rowe SP, Calais J, Hofman MS, Maurer T, Schwarzenboeck SM, Kratochwil C, Herrmann K, Giesel FL. Prostate-Specific Membrane Antigen Ligands for Imaging and Therapy. *J Nucl Med*. 2017; 58:67S-76S. <https://doi.org/10.2967/jnumed.116.186767>.
9. Pyka T, Okamoto S, Dahlbender M, Tauber R, Retz M, Heck M, Tamaki N, Schwaiger M, Maurer T, Eiber M. Comparison of bone scintigraphy and 68Ga-PSMA PET for skeletal staging in prostate cancer. *Eur J Nucl Med Mol Imaging*. 2016; 43:2114-21. <https://doi.org/10.1007/s00259-016-3435-0>.
10. Rowe SP, Macura KJ, Mena E, Blackford AL, Nadal R, Antonarakis ES, Eisenberger M, Carducci M, Fan H, Dannals RF, Chen Y, Mease RC, Szabo Z, et al. PSMA-Based [(18F)]DCFPyL PET/CT Is Superior to Conventional Imaging for Lesion Detection in Patients with Metastatic Prostate Cancer. *Mol Imaging Biol*. 2016; 18:411-9. <https://doi.org/10.1007/s11307-016-0957-6>.
11. Rowe SP, Mana-Ay M, Javadi MS, Szabo Z, Leal JP, Pomper MG, Pienta KJ, Ross AE, Gorin MA. PSMA-Based Detection of Prostate Cancer Bone Lesions With 18F-DCFPyL PET/CT: A Sensitive Alternative to (99m) Tc-MDP Bone Scan and Na18F PET/CT? *Clin Genitourin Cancer*. 2016; 14:e115-8. <https://doi.org/10.1016/j.clgc.2015.09.011>.
12. Harmon SA, Bergvall E, Mena E, Shih JH, Adler S, McKinney Y, Mehralivand S, Citrin DE, Couvillon A, Madan R, Gulley J, Mease RC, Jacobs PM, et al. A Prospective Comparison of 18 F-Sodium Fluoride PET/CT and PSMA-targeted 18 F-DCFBC PET/CT in Metastatic Prostate Cancer. *J Nucl Med*. 2018; 59:1665-71. <https://doi.org/10.2967/jnumed.117.207373>.
13. Uprimny C, Sviriydenka A, Fritz J, Kroiss AS, Nilica B, Decristoforo C, Haubner R, von Guggenberg E, Buxbaum S, Horninger W, Virgolini JJ. Comparison of [68 Ga] Ga-PSMA-11 PET/CT with [18F]NaF PET/CT in the evaluation of bone metastases in metastatic prostate cancer patients prior to radionuclide therapy. *Eur J Nucl Med Mol Imaging*. 2018; 45:1873-83. <https://doi.org/10.1007/s00259-018-4048-6>.
14. Janssen JC, Meißner S, Woythal N, Prasad V, Brenner W, Diederichs G, Hamm B, Makowski MR. Comparison of hybrid 68Ga-PSMA-PET/CT and 99mTc-DPD-SPECT/CT for the detection of bone metastases in prostate cancer patients: additional value of morphologic information from low dose CT. *Eur Radiol*. 2018; 28:610-19. <https://doi.org/10.1007/s00330-017-4994-6>
15. Roudier MP, Vesselle H, True LD, Higano CS, Ott SM, King SH, Vessella RL. Bone histology at autopsy and matched bone scintigraphy findings in patients with hormone refractory prostate cancer: the effect of bisphosphonate therapy on bone scintigraphy results. *Clin Exp Metastasis*. 2003; 20:171-80.
16. Holmes MG, Foss E, Joseph G, Foye A, Beckett B, Motamedi D, Youngren J, Thomas GV, Huang J, Aggarwal R, Alumkal JJ, Beer TM, Small EJ, Link TM. CT-Guided Bone Biopsies in Metastatic Castration-Resistant Prostate Cancer: Factors Predictive of Maximum Tumor Yield. *J Vasc Interv Radiol*. 2017; 28:1073-81.e1. <https://doi.org/10.1016/j.jvir.2017.04.019>.
17. Roudier MP, Morrissey C, True LD, Higano CS, Vessella RL, Ott SM. Histopathological assessment of prostate

- cancer bone osteoblastic metastases. *J Urol.* 2008; 180:1154-60. <https://doi.org/10.1016/j.juro.2008.04.140>.
18. Oldan JD, Hawkins AS, Chin BB. (18)F Sodium Fluoride PET/CT in Patients with Prostate Cancer: Quantification of Normal Tissues, Benign Degenerative Lesions, and Malignant Lesions. *World J Nucl Med.* 2016; 15:102-8. <https://doi.org/10.4103/1450-1147.172301>.
 19. Nishimori H, Ehata S, Suzuki HI, Katsuno Y, Miyazono K. Prostate cancer cells and bone stromal cells mutually interact with each other through bone morphogenetic protein-mediated signals. *J Biol Chem.* 2012; 287:20037-46. <https://doi.org/10.1074/jbc.M112.353094>.
 20. Larson SR, Zhang X, Dumpit R, Coleman I, Lakely B, Roudier M, Higano CS, True LD, Lange PH, Montgomery B, Corey E, Nelson PS, Vessella RL, Morrissey C. Characterization of osteoblastic and osteolytic proteins in prostate cancer bone metastases. *Prostate.* 2013; 73:932-40. <https://doi.org/10.1002/pros.22639>.
 21. Shiao SL, Chu GC, Chung LW. Regulation of prostate cancer progression by the tumor microenvironment. *Cancer Lett.* 2016; 380:340-8. <https://doi.org/10.1016/j.canlet.2015.12.022>.
 22. Pinski J, Parikh A, Bova GS, Isaacs JT. Therapeutic implications of enhanced G(0)/G(1) checkpoint control induced by coculture of prostate cancer cells with osteoblasts. *Cancer Res.* 2001; 61:6372-6.
 23. Scher HI, Solo K, Valant J, Todd MB, Mehra M. Prevalence of Prostate Cancer Clinical States and Mortality in the United States: Estimates Using a Dynamic Progression Model. *PLoS One.* 2015; 10:e0139440. <https://doi.org/10.1371/journal.pone.0139440>.
 24. Roudier MP, True LD, Higano CS, Vesselle H, Ellis W, Lange P, Vessella RL. Phenotypic heterogeneity of end-stage prostate carcinoma metastatic to bone. *Hum Pathol.* 2003; 34:646-53. [https://doi.org/10.1016/S0046-8177\(03\)00190-4](https://doi.org/10.1016/S0046-8177(03)00190-4)
 25. Cook GJ, Houston S, Rubens R, Maisey MN, Fogelman I. Detection of bone metastases in breast cancer by 18FDG PET: differing metabolic activity in osteoblastic and osteolytic lesions. *J Clin Oncol.* 1998; 16:3375-9. <https://doi.org/10.1200/JCO.1998.16.10.3375>.
 26. Peterson LM, O'Sullivan J, Wu QV, Novakova-Jiresova A, Jenkins I, Lee JH, Shields A, Montgomery S, Linden HM, Gralow JR, Gadi VK, Muzi M, Kinahan PE, et al. Prospective study of serial. *J Nucl Med.* 2018; 59:1823-30. <https://doi.org/10.2967/jnumed.118.211102>
 27. Parker C, Nilsson S, Heinrich D, Helle SI, O'Sullivan JM, Fosså SD, Chodacki A, Wiechno P, Logue J, Seke M, Widmark A, Johannessen DC, Hoskin P, et al, and ALSYMPCA Investigators. *N Engl J Med.* 2013; 369:213-23. <https://doi.org/10.1056/NEJMoa1213755>.
 28. Murray I, Chittenden SJ, Denis-Bacelar AM, Hindorf C, Parker CC, Chua S, Flux GD. The potential of 223Ra and 18F-fluoride imaging to predict bone lesion response to treatment with 223Ra-dichloride in castration-resistant prostate cancer. *Eur J Nucl Med Mol Imaging.* 2017; 44:1832-44. <https://doi.org/10.1007/s00259-017-3744-y>.
 29. Simoncic U, Perlman S, Liu G, Staab MJ, Straus JE, Jeraj R. Comparison of NaF and FDG PET/CT for assessment of treatment response in castration-resistant prostate cancers with osseous metastases. *Clin Genitourin Cancer.* 2015; 13:e7-e17. <https://doi.org/10.1016/j.clgc.2014.07.001>.
 30. Zukotynski KA, Kim CK, Gerbaudo VH, Hainer J, Taplin ME, Kantoff P, den Abbeele AD, Seltzer S, Sweeney CJ. (18)F-FDG-PET/CT and (18)F-NaF-PET/CT in men with castrate-resistant prostate cancer. *Am J Nucl Med Mol Imaging.* 2015; 5:72-82.
 31. Vargas HA, Wassberg C, Fox JJ, Wibmer A, Goldman DA, Kuk D, Gonen M, Larson SM, Morris MJ, Scher HI, Hricak H. Bone metastases in castration-resistant prostate cancer: associations between morphologic CT patterns, glycolytic activity, and androgen receptor expression on PET and overall survival. *Radiology.* 2014; 271:220-9. <https://doi.org/10.1148/radiol.13130625>.
 32. Beheshti M, Vali R, Waldenberger P, Fitz F, Nader M, Hammer J, Loidl W, Pirich C, Fogelman I, Langsteger W. The use of F-18 choline PET in the assessment of bone metastases in prostate cancer: correlation with morphological changes on CT. *Mol Imaging Biol.* 2009; 11:446-54. <https://doi.org/10.1007/s11307-009-0217-0>.
 33. Bettinardi V, Castiglioni I, De Bernardi E, Gilardi MC. PET quantification: strategies for partial volume correction. *Clin Transl Imaging.* 2014; 2:199-218. <https://doi.org/10.1007/s40336-014-0066-y>.
 34. Surti S, Kuhn A, Werner ME, Perkins AE, Kolthammer J, Karp JS. Performance of Philips Gemini TF PET/CT scanner with special consideration for its time-of-flight imaging capabilities. *J Nucl Med.* 2007; 48:471-80.
 35. Ravert HT, Holt DP, Chen Y, Mease RC, Fan H, Pomper MG, Dannals RF. An improved synthesis of the radiolabeled prostate-specific membrane antigen inhibitor, [(18) F] DCFPyL. *J Labelled Comp Radiopharm.* 2016; 59:439-50. <https://doi.org/10.1002/jlcr.3430>.
 36. Rosner B, Glynn RJ, Lee ML. Extension of the rank sum test for clustered data: two-group comparisons with group membership defined at the subunit level. *Biometrics.* 2006; 62:1251-9. <https://doi.org/10.1111/j.1541-0420.2006.00582.x>.